

Quantum vortex reconnections: crossover from interaction to driven regimes

Luca Galantucci,^{1,*} A. W. Baggaley,¹ N. G. Parker,¹ and C. F. Barenghi¹

¹*Joint Quantum Centre (JQC) Durham–Newcastle,
and School of Mathematics and Statistics, Newcastle University,
Newcastle upon Tyne, NE1 7RU, United Kingdom*

(Dated: December 15, 2024)

Reconnections of coherent filamentary structures play a key role in the dynamics of fluids, redistributing energy and helicity among the length scales, triggering dissipative effects and inducing fine-scale mixing. Unlike ordinary (classical) fluids where vorticity is a continuous field, in superfluid helium and in atomic Bose-Einstein condensates (BECs) vorticity takes the form of isolated quantised vortex lines, which are conceptually easier to study. New experimental techniques now allow visualisation of individual vortex reconnections in helium and condensates. It has long been suspected that reconnections obey universal laws, particularly a universal scaling with time of the minimum distance between vortices δ . Here we perform a comprehensive analysis of this scaling across a range of scenarios relevant to superfluid helium and trapped condensates, combining our own numerical simulations with the previous results in the literature. We reveal that the scaling exhibit two distinct regimes: a $\delta \sim t^{1/2}$ scaling arising from the mutual interaction of the reconnecting strands and a $\delta \sim t$ scaling when extrinsic factors drive the individual vortices.

RECONNECTIONS IN CLASSICAL AND QUANTUM SYSTEMS

Reconnections of coherent filamentary structures (Fig. 1) play a fundamental role in the dynamics of plasmas (from astrophysics [1–3] to confined nuclear fusion), nematic liquid crystals [4], polymers and macromolecules [5] (including DNA [6]), optical beams [7, 8], ordinary (classical) fluids [9–11] and quantum fluids [12, 13]. In fluids, the coherent structures consist of concentrated vorticity, whose character depends on the classical or quantum nature of the fluid: in classical fluids (air, water etc.), vorticity is a continuous field and the interacting structures are *vortex tubes* of arbitrary core size around which the circulation of the velocity field is unconstrained; in quantum fluids (atomic Bose-Einstein Condensates (BECs), and superfluid ^4He and ^3He), the structures are isolated one-dimensional *vortex lines*, corresponding to topological defects of the governing order parameter around which the velocity’s circulation is quantized [14–17].

The discrete nature of quantum vortices makes them ideal for the study of vortex reconnections, which assume the form of isolated, dramatic events, strongly localised in space and time. First conjectured by Feynman [15] and then numerically predicted [19], quantum vortex reconnections been observed only recently, both in superfluid ^4He [20] (indirectly, using tracer particles) and in BECs [21] (directly, using an innovative stroboscopic visualisation technique).

Vortex reconnections are crucial in redistributing the kinetic energy of turbulent superfluids. In some regimes, they trigger a turbulent energy cascade [22] in which vortex lines self-organise in bundles [23], generating the same Kolmogorov spectrum of classical turbulence [22, 24–27].

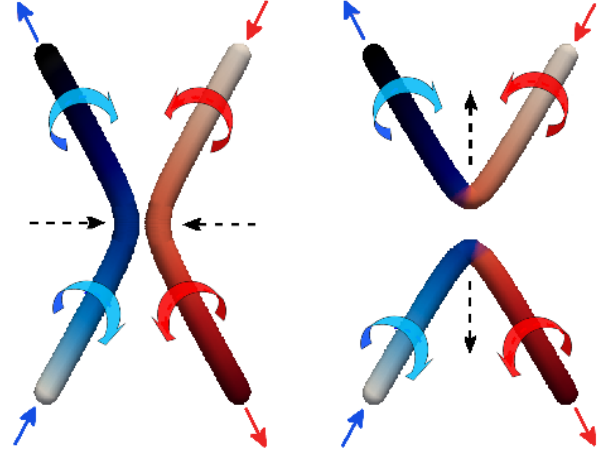


FIG. 1. **Reconnecting vortex lines exchanging strands.** Schematic vortex configurations before the reconnection (left) and after (right); the vortices’ shape is as determined analytically by Nazarenko and West [18]. Color gradient along the vortices and blue/red arrows indicate the directions of the vorticity along the vortices and the direction of the flow velocity around them. Dashed black arrows indicate the vortex motion, first towards each others, then away from each others.

By altering the topology of the flow [28], reconnections also seem to redistribute its helicity [29, 30], although the precise definition of helicity in superfluids is currently debated [30–32], and the effects of reconnections [33–36] on its geometric ingredients (link, writhe and twist) are still discussed. In the low-temperature limit, viscous or friction losses are negligible, and reconnections are the ultimate mechanism for the dissipation of the incompressible kinetic energy of the superfluid via sound radiation at the reconnecting event [37, 38] followed by further sound emission by the Kelvin wave cascade [39–41] which fol-

lows the relaxation of the reconnection cusps.

IS THERE A UNIVERSAL ROUTE TO RECONNECTION ?

Many authors have focused on the possibility that there is a *universal route* to reconnection, which may take the form of a vortex ring cascade [42, 43], a particular rule for the cusp angles [44, 45], or, more promising, a special scaling with time of the minimum distance $\delta(t)$ between the reconnecting vortex strands. It is on the last property that we concentrate our attention.

Several studies have observed a symmetrical pre/post reconnection scaling of $\delta(t)$ [18, 44, 46–48]; others have suggested an asymmetrical scaling ascribed to acoustic energy losses [38, 49, 50], similar to the asymmetry observed in classical Navier-Stokes fluids [51]. In Fig. 2 we present a comprehensive summary of the scaling of $\delta(t)$, combining previous numerical and experimental results with data computed in the present study; this spans an impressive eight orders of magnitude.

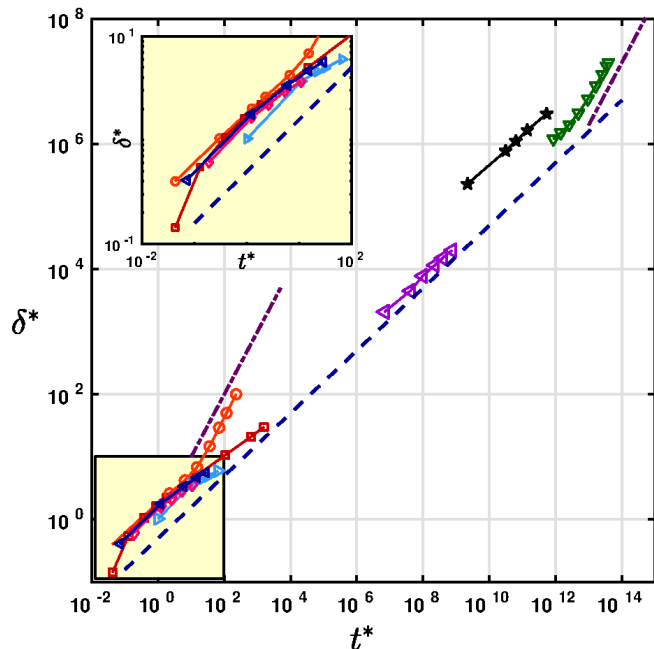


FIG. 2. **Minimum distance between reconnecting vortices: past and present results.** All data reported describe the behaviour of the rescaled minimum distance δ^* between vortices as a function of the rescaled temporal distance to the reconnection event t^* . Empty (filled) symbols refer to pre (post) - reconnection dynamics. **GP simulations:** \blacktriangleright Ref. [50]; \blacktriangleleft Ref. [48]; \blacklozenge Ref. [38]; \circ and \square , present simulations, ring-vortex collision and orthogonal reconnection, respectively. **VFM simulations:** \blacktriangleleft Ref. [44]; \blacktriangledown present simulations, ring-line collision. **Experiments:** \star Ref. [46].

The aim of this paper is to reveal that there are *two* distinct scaling regimes for $\delta(t)$. In addition to the known

[18, 44, 46–48] $\delta \sim t^{1/2}$ scaling, we predict and observe a new linear scaling $\delta(t) \sim t$. We show how the two scalings arise from rigorous dimensional arguments, then demonstrate them in numerical simulations of vortex reconnections

DIMENSIONAL ANALYSIS

We conjecture that, in the system under consideration (superfluid helium, atomic BECs), δ depends only upon the following physical variables: the time t from the reconnection, the quantum of circulation κ of the superfluid, a characteristic lengthscale ℓ associated to the geometry of the vortex configuration, the fluid’s density ρ , and the density gradient $\nabla\rho$. We hence postulate the following functional form

$$f(\delta, t, \kappa, \ell, \rho, \nabla\rho) = 0. \quad (1)$$

Following the standard procedure of the Buckingham π -theorem [52] (see Supporting Information SI.1 for details), we derive the following scalings:

$$\delta(t) = (C_1\kappa)^{1/2}t^{1/2} \quad \text{interaction regime}, \quad (2)$$

$$\delta(t) = C_2\left(\frac{\kappa}{\ell}\right)t \quad \text{driven regime}, \quad (3)$$

$$\delta(t) = C_3\left(\kappa\frac{\nabla\rho}{\rho}\right)t \quad \text{driven regime}, \quad (4)$$

where C_1 , C_2 and C_3 are dimensionless constants. Physically, the $\delta \sim t^{1/2}$ scaling of Eq. (2) identifies the quantum of circulation κ as the only relevant parameter driving the reconnection dynamics [20].

Equations (3, 4), however, introduce the new $\delta \sim t$ scaling. This scaling suggests the presence of a characteristic velocity which drives the approach/separation of the vortex lines. Indeed, we can offer some physical examples of these velocities. If ℓ is the radius of a vortex ring, then $v_\ell = C_2(\kappa/\ell)$ is, to a first approximation, the self-induced velocity of the ring. Alternatively, if ℓ is equal to the distance of a vortex to a sharp boundary in an otherwise homogeneous BEC (such as arises for BEC confined by box traps), then v_ℓ is the self-induced vortex velocity arising from the presence of an image vortex. Finally, if the BEC density is smoothly-varying (such as arises for BECs confined by harmonic traps) then $v_{\nabla\rho} = C_3(\kappa\nabla\rho/\rho)$ is precisely the individual velocity of a vortex induced by the density gradients, C_3 depending on the trap’s geometry [53, 54]. In the next section we will see how these scalings, and the crossover, emerge in typical scenarios through numerical simulations.

NUMERICAL SIMULATIONS

There are two established models of quantum vortex dynamics: the Gross-Pitaevskii (GP) model and the Vortex Filament (VF) method. The former describes a weakly-interacting BEC in the zero-temperature limit [55], the latter is based on the classical Biot-Savart law describing the velocity field of a given vorticity distribution, which in our case is concentrated on space curves [56, 57].

The main difference between GP and VF models is the probed lengthscales of the flow. The GP equation is a *microscopic*, compressible model, capable of describing density fluctuations and lengthscales smaller than the vortex core a_0 . In the GP model, vortices are identified as topological phase defects of the condensate wavefunction Ψ , and reconnections are solutions of the GP equation itself. On the other hand, the VF method is a *mesoscopic* incompressible model, probing the features of the flow at lengthscales much larger than the vortex core, typically $10^4 a_0$ or $10^5 a_0$, neglecting any density perturbation created by moving vortices and the density depletions represented by the vortex cores themselves. In the VF model, vortex lines are discretised employing a set of Lagrangian points whose dynamics is governed by the classical Biot-Savart law, and vortex reconnections are performed by an *ad hoc* ‘cut-and-paste’ algorithm [56, 58].

In the present study, we employ both GP and VF models to investigate the scaling with time of the minimum distance δ between reconnecting vortices. Technical details of these methods are described in Supporting Information SI.5. Distinctive of our simulations is the larger initial distance δ_0 compared to past numerical studies (5 to 20 times larger in GP simulations, 100 to 1000 larger in VF ones). We also extend the use of the GP model to inhomogeneous, confined BECs where vortex reconnections can now be investigated experimentally with unprecedented resolution [21].

Homogeneous unbounded systems

The first case which we consider is when reconnecting vortices are initially orthogonal to each other. This set-up, and the results for $\delta(t)$, are shown in Fig. 3 (left) and reported in movies M1. Previous GP simulations of this geometry used initial distances $\delta_0 \lesssim 6\xi$, where $\xi = \hbar/\sqrt{2mgn}$ is the healing length of the system ($a_0 \approx 4\xi$ to 5ξ), and m , g and n are the boson mass, the repulsive strength of boson interaction and the density of bosons respectively. Here we extend the investigations to initial distances $\delta_0 \approx 30\xi$. Introducing the rescaled distance $\delta^* = \delta/\xi$ and time $t^* = |t - t_r|/\tau$ (where t_r is the reconnection instant and $\tau = \xi/c$, $c = \sqrt{gn/m}$ being the speed of sound in a homogeneous BEC), we observe that for $\delta^* \lesssim 5$ (when the vortex cores start merging)

a symmetrical $t^{*1/2}$ scaling emerges clearly for both pre- and post-reconnection dynamics. This is consistent with recent GP simulations [48] and in conflict with other numerical GP studies [38, 50]. For larger distances, this $t^{*1/2}$ scaling still holds for post-reconnection dynamics, while the exponent slightly decreases in the approach dynamics due to the slow initial vortex motion. As pointed out in past studies [38, 48–50], we find that the vortex lines move faster after the reconnection than before it. The pre-reconnection motion is very similar for all three initial distances δ_0 . However, we note the slight deviation from the $t^{1/2}$ behaviour at early times, obviously influenced by the initial conditions, and the slight sensitivity to the initial distance δ_0^* .

The second case which we consider is a vortex ring reconnecting with an isolated initially straight vortex line (see movies M2). Figure 3 (right) illustrates this scenario and presents the behaviour of $\delta(t)$. We vary the initial radius of the ring ($R_0^* = R_0/\xi = 5, 7.5$ and 10), while keeping constant its initial distance $\delta_0^* = 100$ to the line.

We first focus on the pre-reconnection evolution of $\delta(t)$. This clearly reveals the two distinct scalings predicted by the dimensional analysis:

$$\delta^*(t^*) \sim a_{1/2} t^{*1/2} \quad \text{for } t^* \lesssim 5, \quad (5)$$

$$\delta^*(t^*) \sim a_1 t^* \quad \text{for } t^* \gtrsim 20, \quad (6)$$

where $a_{1/2}$ and a_1 are constant prefactors corresponding, respectively, to $(C_1\kappa)^{1/2}$ in Eq. (2) and v_ℓ or $v_{\nabla\rho}$ in Eqs. (3) or (4). To our knowledge, the linear scaling has not been reported in previous studies. We also note that the crossover between these two regimes occurs at a distance of $\delta_c \sim 5\xi$; we will revisit the importance of this scale later.

The linear scaling implies that $d\delta^*/dt^*$ is constant: at large distances, the relative velocity between the two points at minimum distance, \mathbf{x}_{ring} (on the vortex ring) and \mathbf{x}_{line} (on the vortex line), projected on the separation vector $\boldsymbol{\delta} = \mathbf{x}_{\text{ring}} - \mathbf{x}_{\text{line}}$, is constant with respect to time. We argue that, at large separation distances $d\delta^*/dt^*$ is approximately equal to the initial speed of the vortex ring [59]:

$$\frac{d\delta^*}{dt^*} = v_{\text{ring}}^* = \frac{\kappa}{4\pi\xi c R_0^*} \left[\ln(8R_0^*) - 0.615 \right]. \quad (7)$$

The self-induced velocity of the vortex ring v_{ring} thus plays the role of the characteristic velocity v_ℓ in Eq. (3). We make the notation compact and rewrite Eq. (7) as $v_{\text{ring}}^* = Cf(\tilde{R}_0)$, where $C = \kappa/(4\pi c \bar{R}_0)$, $f(\tilde{R}_0) = [\ln(\tilde{R}_0) + 3.48]/\tilde{R}_0$, $\bar{R}_0 = 7.5\xi$ is the average radius of the three simulations, and $\tilde{R}_0 = R_0/\bar{R}_0$. We then arrive at the result that Eq. (6) takes the form $\delta^*(t^*) \sim Cf(\tilde{R}_0)t^*$. This is confirmed in Fig. 3 (right, inset): when δ^* is rescaled as $\delta^*/f(\tilde{R}_0)$ the curves collapse onto a single curve in the $\delta \sim t$ regime.

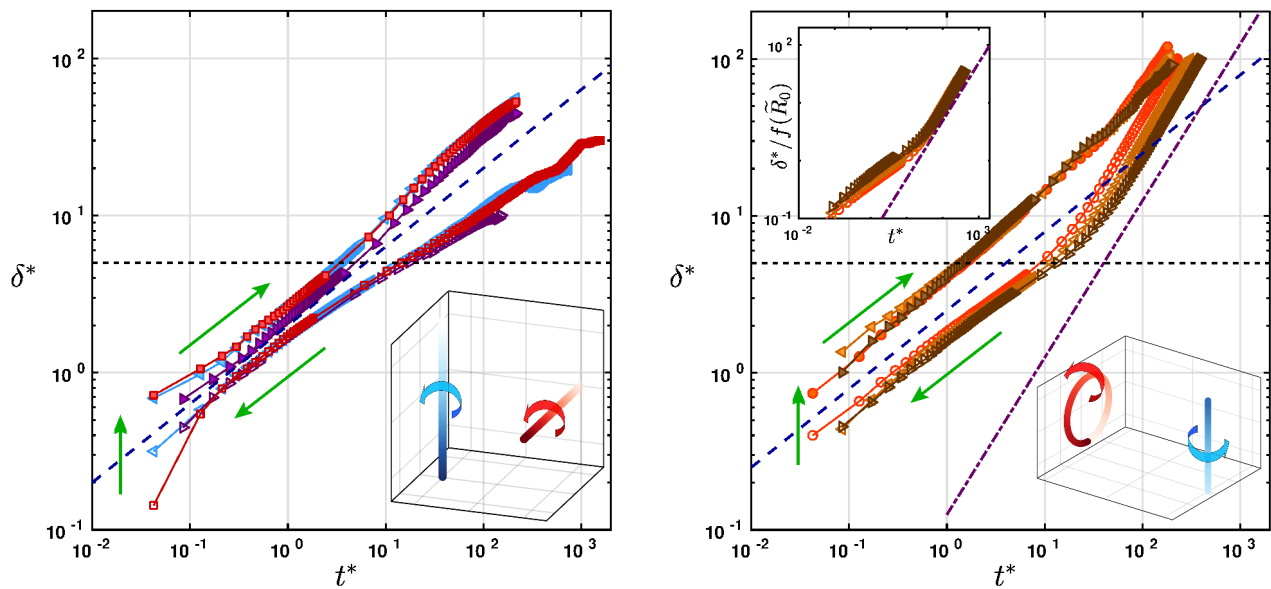


FIG. 3. **GP simulations: homogeneous unbounded BECs.** Evolution of the rescaled minimum distance δ^* between reconnecting vortices as a function of the rescaled temporal distance to reconnection t^* . Empty (filled) symbols correspond to pre (post) reconnection dynamics. **Left:** orthogonal vortices reconnection with rescaled initial distance δ_0^* equal to 10 (\blacktriangleright), 20 (\blacktriangleleft) and 30 (\blacksquare). **Right:** ring-line reconnection for constant initial distance $\delta_0^* = 100$ and vortex ring radii R_0^* equal to 5 (\circ), 7.5 (\blacktriangleleft) and 10 (\blacktriangleright). **Inset:** pre-reconnection dynamics only, the distance is rescaled with $f(\tilde{R}_0)$. In both sub figures: the horizontal dashed black line indicates the width of the vortex core ($\approx 5\xi$), the blue-dashed line shows the $t^{*1/2}$ scaling and the bottom insets show the initial vortex configuration. Color gradient on vortices indicates direction of the superfluid vorticity (from light to dark). Dot-dashed violet line in the right panel indicates the t^* scaling. Green arrows indicate the direction of time.

The clear $t^{*1/2}$ scaling for $\delta^* \lesssim 5$ is consistent with that seen for the orthogonal reconnection. This is to be expected: at sufficiently small distances, the approach/separation is governed by the mutual interaction of the two vortices, $d\delta^*/dt^* \propto \kappa/(4\pi\delta^*)$ [44], leading straightforwardly to the scaling $\delta^* \sim t^{*1/2}$.

We suggest that these two scalings correspond to a crossover from interaction-dominated motion of the reconnecting strands ($\delta^* \sim t^{*1/2}$ scaling) to the self-driven (curvature-driven) motion of the ring ($\delta^* \sim t^*$ scaling). To check this conjecture, Fig. 4 shows the contribution of the local vortex curvature v_γ to the approach velocity $d\delta^*/dt^*$ for ring-line reconnections (see Supporting Information SI.2 for the calculation of v_γ). We see that the contribution from the local vortex curvature to the approach velocity drops dramatically for $t^* \lesssim 10$, corresponding exactly to the onset of the $t^{*1/2}$ scaling, supporting this picture.

The crossover between the two scalings, however, is less apparent in the post-reconnection dynamics, and for two main reasons. Firstly, both vortices become perturbed by propagating Kelvin-waves; secondly, the travelling velocity of the perturbed vortex ring is not constant [60–62]. These Kelvin waves generate sound waves [63, 64] dissipating the incompressible kinetic energy, leading to a decrease of the length of the vortex ring and a damping

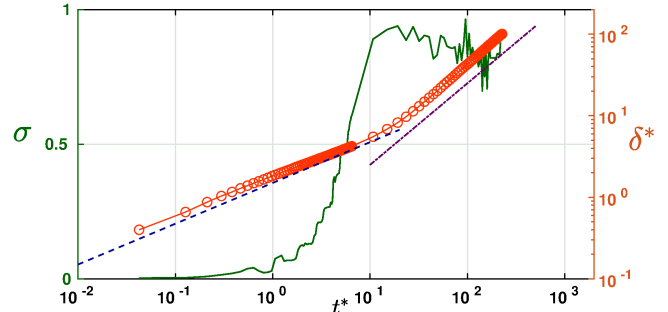


FIG. 4. **Curvature contribution.** Temporal evolution of the ratio $\sigma = v_\gamma / (d\delta^*/dt^*)$ (green solid line) and rescaled minimum distance δ^* (orange circles) for the ring-line pre-reconnection, with $R_0^* = 5$. The blue-dashed line shows the $t^{*1/2}$ scaling, while dot-dashed violet line indicates the t^* scaling.

of the oscillations' amplitude. When these oscillations die out (*e.g.* in the simulation with $R_0^* = 5$, see Fig. 3 (right)), and the vortex ring regains its circular shape travelling at constant velocity away from the vortex line, we recover the expected $\delta^* \sim t^*$ scaling.

The same qualitative behaviour for the orthogonal vortices and ring-line scenario is recovered in VF simulations (see Supporting Information SI.3, Fig. S1). However, in the latter scenario, the crossover from $t^{*1/2}$ to

t^* scaling occurs at a larger lengthscale than in the GP simulations. Here, the distance δ_c at which the crossover takes place is determined by the spatial resolution $\Delta\zeta$ used to discretize the vortex lines, which constrains the smallest numerically-resolved radius of curvature to $R_{c,\min} \sim 5\Delta\zeta$, hence limiting the maximum curvature-driven velocity. As a consequence, when the minimum distance δ is smaller than the threshold distance $\delta_c \sim R_{c,\min} \gg \xi$, the interaction regimes still prevails, producing $t^{*1/2}$ scaling even at distances much larger than the healing length.

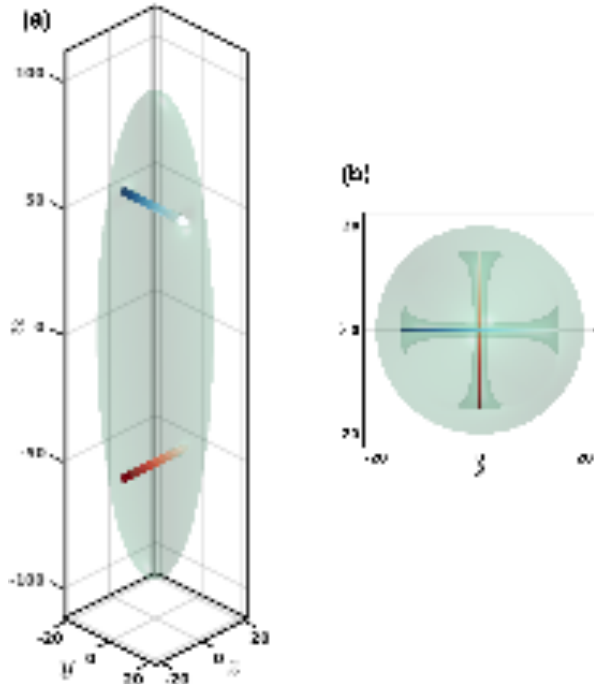


FIG. 5. **GP simulations: harmonically trapped BECs, initial conditions.** (a), (b): Lateral and top view of initial vortex configuration. Light green surfaces are isosurfaces of condensate density at 5% of trap-center density. Color gradient on vortices indicates the direction of the superfluid vorticity (from light to dark). Unit of length is the healing length ξ_c evaluated in the center of the trap.

Trapped systems

Since it is now experimentally possible to visualise individual quantum reconnections in trapped atomic BECs [21, 65], we test the above results under such realistic experimental set-ups. We consider two classes of traps: the widely-employed *harmonic traps* [66] (Figs. 5 and 6 and movies M3) and the recently-designed *box-traps* [67, 68] (see Supportive Information SI.4 and movies M4). We employ GP simulations throughout this analysis (the VF model is not suitable for inhomogeneous systems).

In harmonic traps the condensate is inhomogeneous

(the density is larger near the centre) and individual motion of the vortices (responsible for the linear scaling) is determined by their curvature and the density gradients [53, 54, 69]. In box-traps the condensate's density is constant (with the exception of a thin layer of width of the order of the healing length near the boundary), and the individual vortex motion is driven by image vortices with respect to the boundaries [70]. We exploit these self-driven vortex motions to analyse reconnections starting from initial distances significantly larger than previous numerical simulations (up to 20 times larger).

Consider first the harmonic trap case; the initial configuration is shown in Fig. 5. The condensate is taken to be cigar-shaped, with the long axis along x (the trapping frequency ω_x along x is smaller than those in the transverse directions, $\omega_y = \omega_z = \omega_\perp$). In this geometry, a single straight vortex line imprinted off center on a radial plane is known to orbit around the center of the condensate [71, 72] along an elliptical orbit perpendicular to itself. The vortex follows a trajectory of constant energy [54] which is uniquely determined by the orbit parameter $\chi = x_0/R_x = r_0/R_\perp$, where x_0 and r_0 are the axial and radial semi-axes of the ellipse, and R_x and R_\perp are the axial and radial Thomas-Fermi radii respectively. The period T of this orbit decreases with increasing χ [54, 65, 73–75], $T = \frac{8\pi(1-\chi^2)\mu}{3\hbar\omega_\perp\omega_x \ln(R_\perp/\xi_c)}$, where ξ_c is the healing length at the center of the trap. Hence, outer vortices (with larger values of χ) move faster.

If two orthogonal vortices are imprinted on radial planes, intersecting the (long) x axis at opposite positions $\pm x_0$, distinct vortex interactions can occur (vortex rebounds, vortex reconnections, double reconnections, ejections) depending on the value of the orbit parameter χ [21]. Results presented here refer to three different values of χ , all engendering vortex reconnections: $\chi = 0.35, 0.5, 0.6$. The pre-reconnection evolution of $\delta^* = \delta/\xi_c$ is reported in Fig. 6 (left). As for the ring-line reconnection, we observe a cross-over from $t^{*1/2}$ to t^* scaling. This occurs for all values of χ . Moreover, the $t^{*1/2}$ scaling again occurs in the region $\delta^* \lesssim 5$, suggesting that this feature is universal for vortex reconnections in BECs.

If we rescale the minimum distance δ with the healing length ξ_r evaluated at the reconnection point \mathbf{x}_r , $\xi_r = \frac{\hbar}{\sqrt{2gm n_{\text{TF}}(\mathbf{x}_r)}} (n_{\text{TF}}(\mathbf{x}_r))$ being the condensate particle density according to the Thomas-Fermi approximation), the curves corresponding to distinct values of χ overlap for $\delta_r^* = \delta/\xi_r \lesssim 5$ (see the inset of the right panel of Fig. 6). This result implies that ξ_r (hence the radius of the vortex core) is the correct lengthscale which characterises the approach dynamics when vortex cores start merging. Furthermore, the dependence of ξ_r on $mn_{\text{TF}}(\mathbf{x}_r)$ indicates that mass density $\rho = mn$ itself plays a significant role in determining the minimum distance δ

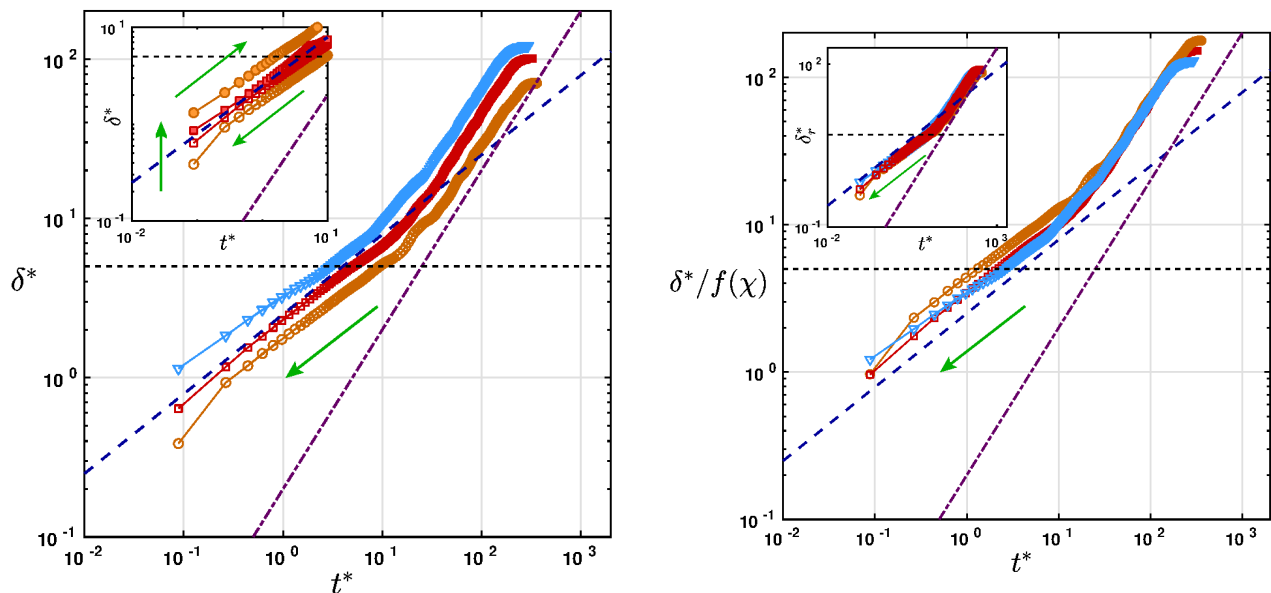


FIG. 6. **GP simulations: harmonically trapped BECs.** Evolution of the minimum distance δ^* between reconnecting vortices as a function of the temporal distance to reconnection t^* . Open (filled) symbols correspond to pre (post) reconnection dynamics. **Left:** pre-reconnection scaling of δ^* for initially imprinted orthogonal vortices with corresponding orbit parameter $\chi = 0.35$ (\circ), $\chi = 0.5$ (\square) and $\chi = 0.6$ (∇). Inset: short-time pre-(open symbols) and post-(filled symbols) reconnection scaling of δ^* for $\chi = 0.35$ (\circ), and $\chi = 0.5$ (\square). **Right:** temporal evolution of the minimum distance δ^* rescaled with $f(\chi)$. Symbols as in left panel. Inset: short-time pre-reconnection scaling of rescaled minimum distance $\delta_r^* = \delta/\xi_r$. In both subfigures, the dashed blue and dot-dashed violet lines show the $t^{*1/2}$ and t^* scalings, respectively. The horizontal dashed line indicates the width of the vortex core at the center of the trap ($\approx 5\xi$). Green arrows indicate the direction of time.

- this is exactly why we included ρ in the set of physical variables when applying Buckingham's π -Theorem.

Another similarity between reconnections in harmonic traps and other geometries is the faster post-reconnection dynamics, as seen in the inset of Fig. 6 (left). This velocity difference between approach and separation (related to an increase of the local vortex curvature in the reconnection process and to an emission of acoustic energy [76]) seems a universal feature of quantum vortex reconnections [48] and also observed in simulations of reconnecting classical vortex tubes [51].

Figure 6 (left) shows that $\frac{d\delta^*}{dt^*}$ is constant for $t^* \gtrsim 20$ before the reconnection, increasing with increasing values of the orbital parameter χ (this is not surprising since isolated vortices move faster on outer orbits). It seems reasonable to assume that $\frac{d\delta^*}{dt^*} = Cf(\chi)$, where $f(\chi) = \frac{\chi}{1-\chi^2}$ and C is a constant which depends on the trap's geometry. Indeed, the magnitude of the vortex velocity induced by both density gradients [54, 69, 77] and vortex curvature (assuming, for simplicity, that the shape of the vortex is an arc of a circle) are proportional to $f(\chi)$. As a consequence, we expect that $\delta^*(t^*) \sim Cf(\chi)t^*$ for $t^* \gtrsim 20$. This conjecture is confirmed in Fig. 6 (right): when plotted as $\delta^*/f(\chi)$, the curves for different χ collapse onto a universal curve in this region. We stress that

although we have numerically identified the dependence of $d\delta^*/dt^*$ on χ at large distances, we still lack a simple physical justification of this result.

In harmonic traps, the predominant effect driving the approach of the vortices at large distances is hence the individual vortex motion driven by curvature and density gradients, independent of the presence of the other vortex. The scaling crossover in harmonic traps is thus governed by the balance between the interaction of the reconnecting strands and the driving of the individual vortices, as it occurs for the ring - line reconnection in homogeneous BECs described previously.

The nature of this scaling crossover is confirmed by the investigation of vortex reconnections in box-trapped BECs, outlined in Supportive Information SI.4 (see, in particular, Fig. S3). In these trapped systems, the motion of individual vortices is driven by vortex images, leading to a linear scaling at large distances. At small distance we again recover the $\delta \sim t^{*1/2}$ scaling. The scaling crossover appears hence to be a universal feature of quantum vortex reconnections when extrinsic factors driving individual vortices exists.

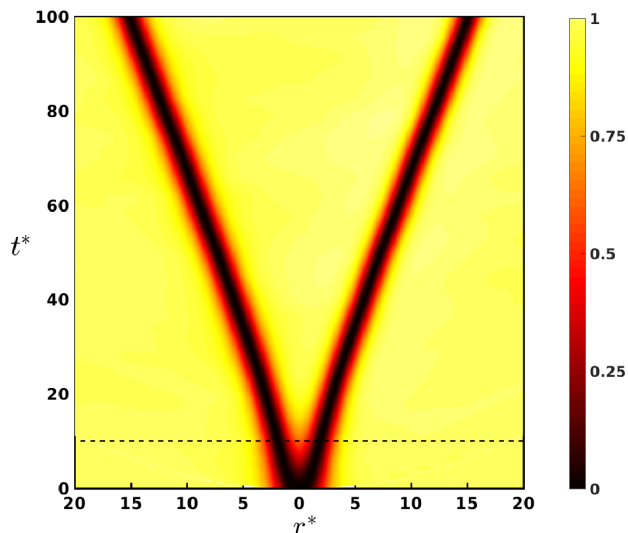


FIG. 7. **The role of density depletions.** Plot of the condensate density along the line containing the separation vector δ between the colliding vortices, as a function of the distance r^* to the mid-point of the separation segment and the rescaled temporal distance to reconnection t^* , for the vortex ring - vortex line pre-reconnection dynamics with $R_0^* = 5$. In the initial phase of the approach (top part of the figure), $\delta \sim t^*$; the cross-over to the $\delta \sim t^{*1/2}$ scaling occurs when the vortex cores start to merge (bottom part) for $t^* \lesssim 10$ (dashed line).

The role of density depletions

Current and previous GP simulations of reconnections in homogeneous and trapped BECs, see a clear symmetric pre/post-reconnection $t^{*1/2}$ scaling in the region $\delta^* \lesssim 5$, irrespective of the initial condition. The effect is robust and mostly went unnoticed, as the prefactors $a_{1/2}$ in Eq. (5) may vary depending on the conditions and between the approach/separation [76]).

Figure 7 shows the condensate density along the line containing the separation vector between two reconnecting vortices (taken to be the ring-line scenario in a homogeneous system), as a function of t^* and the distance $r^* = r/\xi$ to the mid-point of the separation segment. It is clear that for $t^* \lesssim 10$, which is when the $t^{*1/2}$ scaling appears, the density between the two vortices drops dramatically. This behaviour is generic - we obtain it also for any vortex reconnection set-up and across homogeneous and trapped BECs. This result confirms the analytical work of Nazarenko and West [18], who Taylor-expanded the solution of the GP for reconnecting vortex lines and predicted the observed $t^{1/2}$ scaling in this limit of vanishing density (in this limit the cubic nonlinear term vanishes, reducing the GP equation to the linear Schrödinger equation).

CONCLUSIONS

We have addressed the question of whether there is any universal route to quantum vortex reconnections. By applying rigorous dimensional arguments, we have found that the minimum distance between reconnecting vortex lines obeys two universal scaling law regimes: the previously-established $\delta^* \sim t^{*1/2}$ scaling and a new $\delta^* \sim t^*$ scaling, as summarised schematically in Fig. 8. Our conclusion is supported by experiments and computer simulations performed using the two main mathematical models available (the Gross-Pitaevskii equation and Vortex Filament method) across geometries relevant to trapped condensates and superfluid helium and over distances one order of magnitude larger than in previous works. The cross-over between the two regimes is determined by the balance between mutual interaction of the two reconnecting strands and the individual driving of the vortices by extrinsic factors, such as curvature, density gradients and boundaries/images.

Finally, we have found that the $\delta^* \sim t^{*1/2}$ scaling is universally observed as soon as the vortex cores start merging, independently of the initial vortex configuration and trapped potentials (for confined BECs).

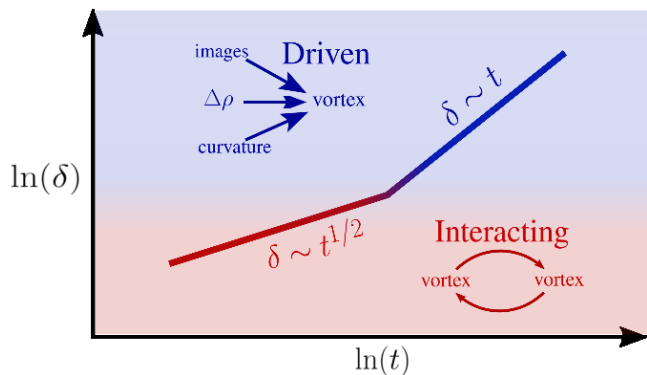


FIG. 8. **Universal routes to the reconnection of two vortex lines.** Top left (red): In the interacting case, the vortex separation δ is determined by the mutual interaction of the two reconnecting vortex strands. Top right (blue): In the driven case, the separate motion of each vortex, hence δ , is set by the background density gradient, or by the presence of images, or by the curvature of the vortex lines. In some vortex configurations, a crossover occurs between these two regimes.

L.G., C.F.B. and N.G.P. acknowledge the support of the Engineering and Physical Sciences Research Council (Grant No. EP/R005192/1).

* luca.galantucci@newcastle.ac.uk

[1] E. Priest and T. Forbes, *Magnetic Reconnection: MHD*

- Theory and Applications* (Cambridge University Press, 2007).
- [2] H. Che, J. Drake, and M. Swisdak, *Nature* **474**, 184 (2011).
 - [3] J. W. Cirtain, L. Golub, A. Winebarger, B. De Pontieu, K. Kobayashi, R. Moore, R. W. Walsh, K. Korreck, M. Weber, P. McCauley, *et al.*, *Nature* **493**, 501 (2013).
 - [4] I. Chuang, R. Durrer, N. Turok, and B. Yurke, *Science* **251**, 1336 (1991).
 - [5] D. Summers, *Notice AMS* **42**, 528 (1995).
 - [6] M. Vazques and D. Summers, *Math Pr Cam Ph Soc* **136**, 565 (2004).
 - [7] M. Dennis, R. King, B. Jack, K. O'Holleran, and M. Padgett, *Nat Phys* **6**, 118 (2010).
 - [8] M. Berry and M. Dennis, *Eur J Phys* **33**, 723 (2012).
 - [9] S. Kida and M. Takaoka, *Annu Rev Fluid Mech* **26**, 169 (1994).
 - [10] A. Pumir and R. Kerr, *Phys Rev Lett* **58**, 1636 (1987).
 - [11] D. Kleckner and W. T. Irvine, *Nat Phys* **9**, 253 (2013).
 - [12] C. Barenghi, R. Donnelly, and W. Vinen, *Quantized vortex dynamics and superfluid turbulence* (Springer, 2001).
 - [13] K. Schwarz, *Phys Rev B* **38**, 2398 (1988).
 - [14] L. Onsager, *Nuovo Cim* **6**, 249 (1949).
 - [15] R. Feynmann, "Application of quantum mechanics to liquid helium," (N Holland Publ Co, 1955) Chap. II, p. 36.
 - [16] W. Vinen, *Proceedings of the Royal Society of London A: Mathematical, Physical and Engineering Sciences*, *Proc Roy Soc London* **260**, 218 (1961).
 - [17] R. J. Donnelly, *Quantized Vortices in Helium II* (Cambridge University Press, 1991).
 - [18] S. Nazarenko and R. West, *J Low Temp Phys* **132**, 1 (2003).
 - [19] J. Koplik and H. Levine, *Phys Rev Lett* **71**, 1375 (1993).
 - [20] G. Bewley, M. Paoletti, K. Sreenivasan, and D. Lathrop, *Proc Natl Acad Sci USA* **105**, 13707 (2008).
 - [21] S. Serafini, L. Galantucci, E. Iseni, T. Bienaime, R. Bisset, C. Barenghi, F. Dalfovo, G. Lamporesi, and G. Ferrari, *Phys Rev X* **7**, 021031 (2017).
 - [22] C. Barenghi, V. L'vov, and P. Roche, *Proc Natl Acad Sci USA* **111**, supp 1, 4683 (2014).
 - [23] A. Baggaley, J. Laurie, and C. Barenghi, *Phys Rev Lett* **109**, 205304 (2012).
 - [24] C. Nore, M. Abid, and M. Brachet, *Phys Rev Lett* **78**, 3896 (1997).
 - [25] L. Skrbek and K. Sreenivasan, *Phys Fluids* **24**, 011301 (2012).
 - [26] J. Maurer and P. Tabeling, *Europhys Lett* **43**, 29 (1998).
 - [27] J. Salort, C. Baudet, B. Castaing, B. Chabaud, F. Daviaud, T. Didelot, P. Diribarne, B. Dubrulle, Y. Gagne, F. Gauthier, A. Girard, B. Henbral, B. Rousset, P. Thibault, and P. E. Roche, *Phys Fluids* **22**, 125102 (2010).
 - [28] D. Kleckner, L. Kauffman, and W. Irvine, *Nat Phys* **12**, 650 (2016).
 - [29] M. Scheeler, D. Kleckner, D. Proment, G. Kindlmann, and W. Irvine, *Proc Natl Acad Sci USA* **111**, 15350 (2014).
 - [30] P. Di Leoni, P. D. Mininni, and M. E. Brachet, *Phys Rev A* **94**, 043605 (2016).
 - [31] H. Salman, *Proc. R. Soc. A* **473**, 20160853 (2017).
 - [32] C. F. Barenghi, L. Galantucci, N. G. Parker, and A. W. Baggaley, *arXiv:1805.09005* (2018).
 - [33] C. Laing, R. Ricca, and D. Summers, *Sci Rep* **5**, 9224 (2015).
 - [34] S. Zuccher and R. Ricca, *Phys Rev E* **92**, 061001 (2015).
 - [35] S. Zuccher and R. L. Ricca, *Phys Rev E* **95**, 053109 (2017).
 - [36] R. Hänninen, N. Hietala, and H. Salman, *Sci Rep* **6**, 37571 (2016).
 - [37] M. Leadbeater, T. Winiecki, D. Samuels, C. Barenghi, and C. Adams, *Phys Rev Lett* **86**, 1410 (2001).
 - [38] S. Zuccher, M. Caliari, A. Baggaley, and C. Barenghi, *Phys Fluids* **24**, 125108 (2012).
 - [39] D. Kivotides, J. Vassilicos, D. Samuels, and C. Barenghi, *Phys Rev Lett* **86**, 3080 (2001).
 - [40] E. Kozik and B. Svistunov, *Phys Rev Lett* **92**, 035301 (2004).
 - [41] E. Kozik and B. Svistunov, *Phys Rev Lett* **94**, 025301 (2005).
 - [42] R. Kerr, *Phys Rev Lett* **106**, 224501 (2011).
 - [43] M. Kurska, K. Bajer, and T. Lipniaki, *Phys Rev B* **83**, 014515 (2011).
 - [44] A. De Waele and R. Aarts, *Phys Rev Lett* **72**, 482 (1994).
 - [45] R. Tebbs, A. J. Youd, and C. Barenghi, *J Low Temp Phys* **162**, 314 (2011).
 - [46] M. Paoletti, M. E. Fisher, and D. Lathrop, *Physica D: Nonlinear Phenomena* **239**, 1367 (2010).
 - [47] F. E. A. dos Santos, *Phys Rev A* **94**, 063633 (2016).
 - [48] A. Villois, D. Proment, and G. Krstulovic, *Phys Rev Fluids* **2**, 044701 (2017).
 - [49] A. Allen, S. Zuccher, M. Caliari, N. Proukakis, N. Parker, and C. Barenghi, *Phys Rev A* **90**, 013601 (2014).
 - [50] C. Rorai, J. Skipper, R. Kerr, and K. Sreenivasan, *J Fluid Mech* **808**, 641 (2016).
 - [51] F. Hussain and K. Duraisamy, *Phys Fluids* **23**, 021701 (2011).
 - [52] E. Buckingham, *Phys Rev* **4**, 345 (1914).
 - [53] B. Jackson, J. McCann, and C. Adams, *Phys Rev A* **61**, 013604 (1999).
 - [54] A. Svidzinsky and A. Fetter, *Phys Rev Lett* **84**, 5919 (2000).
 - [55] L. P. Pitaevskii and S. Stringari, *Bose-Einstein condensation* (Oxford University Press, 2003).
 - [56] K. Schwarz, *Phys Rev B* **31**, 5782 (1985).
 - [57] R. Hänninen and A. W. Baggaley, *Proc Natl Acad Sci USA* , 201312535 (2014).
 - [58] A. W. Baggaley, *J Low Temp Phys* **168**, 18 (2012).
 - [59] P. H. Roberts and J. Grant, *J Phys A: Gen Phys* **4**, 55 (1971).
 - [60] R. Arms and F. R. Hama, *Phys Fluids* **8**, 553 (1965).
 - [61] M. Dhanak and B. D. Bernardinis, *J Fluid Mech* **109**, 189 (1981).
 - [62] C. Barenghi, R. Hänninen, and M. Tsubota, *Phys Rev E* **74**, 046303 (2006).
 - [63] V. Kopiev and S. Chernyshev, *J Fluid Mech* **341**, 19 (1997).
 - [64] N. Parker, N. Proukakis, C. Barenghi, and C. Adams, *Phys Rev Lett* **92**, 160403 (2004).
 - [65] S. Serafini, M. Barbiero, M. Debortoli, S. Donadello, F. Larcher, F. Dalfovo, G. Lamporesi, and G. Ferrari, *Phys Rev Lett* **115**, 170402 (2015).
 - [66] F. Dalfovo, S. Giorgini, L. P. Pitaevskii, and S. Stringari, *Rev Mod. Phys* **71**, 463 (1999).
 - [67] A. Gaunt, T. Schmidutz, I. Gotlibovych, and Z. Smith, R P.Hadzibabic, *Phys Rev Lett* **110**, 200406 (2013).
 - [68] N. Navon, A. Gaunt, and Z. Smith, R P.Hadzibabic, *Nature* **539**, 72 (2016).
 - [69] A. Fetter and A. Svidzinsky, *J. Phys.: Condens. Matter*

- 13**, R135 (2001).
- [70] P. Mason, N. Berloff, and A. Fetter, Phys Rev A **74**, 043611 (2006).
- [71] B. Anderson, P. Haljan, C. Wieman, and E. Cornell, Phys Rev Lett **85**, 2857 (2000).
- [72] D. Freilich, D. Bianchi, A. M. Kaufman, T. Langin, and D. Hall, Science **329**, 1182 (2010).
- [73] E. Lundh and P. Ao, Phys Rev A **61**, 063612 (2000).
- [74] D. Sheehy and L. Radzihovsky, Phys Rev A **70**, 063620 (2004).
- [75] A. Fetter, Rev Mod Phys **81**, 647 (2009).
- [76] A. Villois, G. Krstulovic, and D. Pfroment, (private communication).
- [77] A. Svidzinsky and A. Fetter, Phys Rev A **62**, 063617 (2000).

Quantum vortex reconnections: crossover from interaction to driven regimes

Luca Galantucci,^{1,*} A. W. Baggaley,¹ N. G. Parker,¹ and C. F. Barenghi¹

¹*Joint Quantum Centre (JQC) Durham–Newcastle,
and School of Mathematics and Statistics, Newcastle University,
Newcastle upon Tyne, NE1 7RU, United Kingdom*

(Dated: December 15, 2024)

Supporting Information

SI.1: DIMENSIONAL ANALYSIS

In the main text, we conjectured that the minimum distance δ between reconnecting vortex lines depends upon the temporal distance t to reconnection, the quantum of circulation κ , a characteristic lengthscale ℓ associated to the geometry of the vortex configuration, the density ρ and the density gradient $\nabla\rho$, postulating the existence of a functional relation f such that

$$f(\delta, t, \kappa, \ell, \rho, \nabla\rho) = 0. \quad (1)$$

Following the Buckingham π -Theorem [1], there are only three independent dimensionless quantities, π_1 , π_2 and π_3 , which we choose as: $\pi_1 = \delta^2/(\kappa t)$, $\pi_2 = \ell\delta/(\kappa t)$ and $\pi_3 = \rho\delta/(\kappa t\nabla\rho)$. Other dimensionless quantities can be assembled from the same physical variables, but they would depend on π_1 , π_2 and π_3 .

Eq. (1) can be rewritten as $\pi_1 = F_1(\pi_2, \pi_3)$, or, equivalently, as $\pi_2 = F_2(\pi_1, \pi_3)$, or as $\pi_3 = F_3(\pi_1, \pi_2)$. Choosing $F_1(\pi_2, \pi_3) = C_1$, $F_2(\pi_1, \pi_3) = C_2$ and $F_3(\pi_1, \pi_2) = C_3$ where C_1 , C_2 and C_3 are constant, we find the scalings reported in the main text, namely

$$\delta(t) = (C_1\kappa)^{1/2}t^{1/2}, \quad (2)$$

$$\delta(t) = C_2\left(\frac{\kappa}{\ell}\right)t \quad \text{and} \quad (3)$$

$$\delta(t) = C_3\left(\kappa\frac{\nabla\rho}{\rho}\right)t, \quad (4)$$

where C_1 , C_2 and C_3 are non-dimensional constants. We conclude that there are two distinct scalings: $\delta \sim t^{1/2}$ and $\delta \sim t$.

SI.2: CURVATURE CONTRIBUTION

To find the velocity contribution v_γ arising from the local vortex curvature to the relative approach velocity of the reconnecting vortex lines, $d\delta^*/dt^*$, we proceed as follows. First we compute the velocities $\mathbf{v}_{\gamma,\text{ring}}$ and $\mathbf{v}_{\gamma,\text{line}}$

arising from local vortex curvature of the two points \mathbf{x}_{ring} and \mathbf{x}_{line} on the ring and on the line which correspond to the minimum distance. We assume that each velocity can be approximated by the velocity of a circular vortex ring [2] of radius R_c corresponding to the local curvature $1/R_c$ of that vortex strand, which is obtained by taking suitable derivatives with respect to arc length:

$$\mathbf{v}_{\gamma,\text{line}} = \frac{\kappa}{4\pi R_c} \left[\ln\left(\frac{8R_c}{\xi}\right) - 0.615 \right] \hat{\mathbf{b}}, \quad (5)$$

where $\hat{\mathbf{b}}$ is the unit binormal vector.

Secondly, we project $(\mathbf{v}_{\gamma,\text{ring}} - \mathbf{v}_{\gamma,\text{line}})$ on the separation vector $\boldsymbol{\delta} = \mathbf{x}_{\text{ring}} - \mathbf{x}_{\text{line}}$, obtaining $v_\gamma = (\mathbf{v}_{\gamma,\text{ring}} - \mathbf{v}_{\gamma,\text{line}}) \cdot \hat{\boldsymbol{\delta}}$.

SI.3: VFM SIMULATIONS

Numerical simulations performed using the VFM (Vortex Filament Method) provide further evidence for the scaling laws presented in our article. The VFM [3] applies very well to vortex dynamics in superfluid helium turbulence because of the large separation of scales typical of such problem: $D \gg \ell_v \gg \xi$, where D is the size of the system, ℓ_v the average intervortex distance, and a_0 the vortex core size. When using the VFM to study reconnections of quantum vortices [4]), we must make the following important caveats. Firstly, the VFM does not give information about lengthscales of the order of or smaller than $\Delta\zeta$, defined as the spatial discretisation along the vortex lines; typically, $\Delta\zeta/a_0 \gtrsim 10^5$. Secondly, in the VFM, the motion of vortex line elements is governed by the Biot-Savart law, which formulates the classical Euler equation in integral form. Since vortex reconnections are outside the realm of Euler dynamics, and an ad-hoc artificial *cut and paste* algorithm must be implemented [5] (see Methods for further details). Because of the presence of the reconnections algorithm, the VFM cannot provide physical information at lengthscales smaller than $2\Delta\zeta$ or $3\Delta\zeta$.

Still, information about the minimum vortex distance $\delta(t)$ obtained by the VFM at lengthscales sufficiently larger than $\Delta\zeta$ is important and supports our argu-

ments. In Fig. S1 (left), we report the scaling of δ for initially orthogonal vortices, separated by an initial distance $\delta_0^* = \delta_0/a_0 = 2.5 \times 10^6$. For both pre/post-reconnection dynamics, we only observe the $t^{*1/2}$ scaling, as expected, as the motion of the vortex lines is governed by their mutual interaction.

Fig. S1 (right) illustrates the temporal evolution of δ^* for a ring - line reconnection, and clearly shows the scaling cross-over (arising from the balance between interaction and self-driven motions) which we observe in the corresponding GP simulations. Differently from GP simulations, however, the scale of the cross-over depends on the spatial discretisation $\Delta\zeta$ of vortices, which constrains the smallest radius of curvature $R_{c,min} \sim 5\Delta\zeta$ which is numerically resolved. If $\delta > R_{c,min}$, the dynamics is mainly determined by the self-induced motion of the vortex-ring, leading to $\delta^* \sim t^*$. If $\delta < R_{c,min}$, the dynamics is mainly governed by the interaction between the two vortices, leading to $\delta^* \sim t^{*1/2}$. This crossover is best recognized in the pre-reconnection stage (open symbols) in Fig. S1 (right), where the curve smoothly changes slope; the interpretation of the post-reconnection behaviour (filled symbols) is complicated by the presence of Kelvin waves.

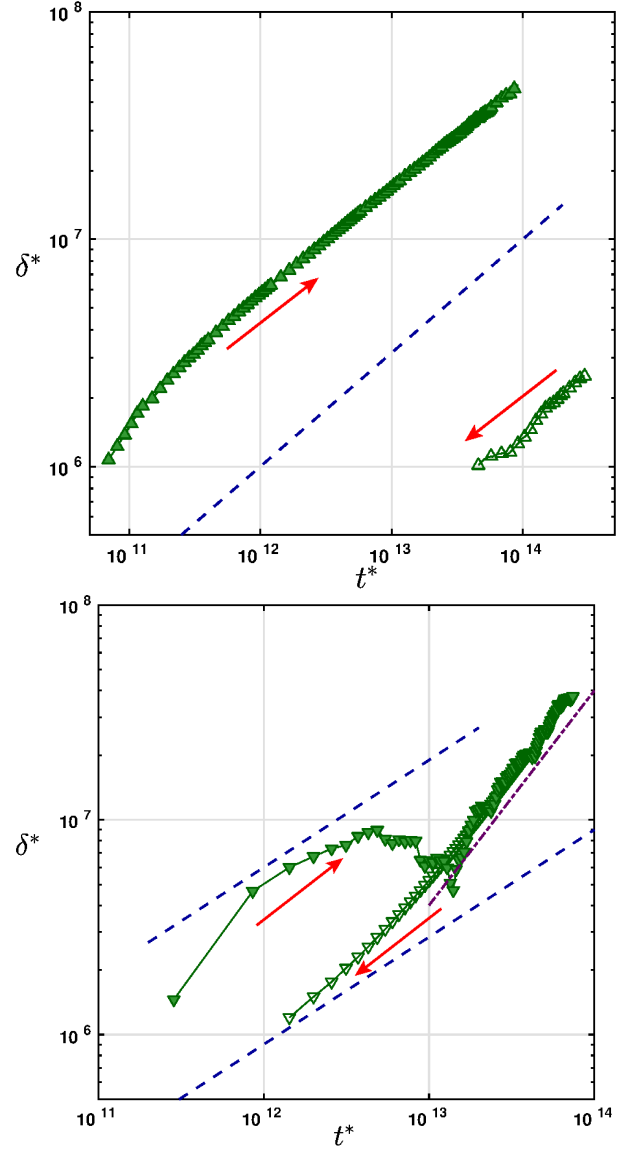


FIG. S1. **VFM simulations: homogeneous, unbounded and incompressible superfluid ^4He systems.** Evolution of the minimum distance δ^* between reconnecting vortices as a function of the temporal distance to reconnection t^* . Open (filled) symbols correspond to pre (post) reconnection dynamics. **Left:** reconnection between initially orthogonal vortices with initial distance $\delta_0^* = 2.5 \times 10^6$. **Right:** vortex-ring - vortex-line reconnection for initial distance $\delta_0^* = 2 \times 10^7$ and vortex-ring initial radius $R_0^* = 1.2 \times 10^7$. In both subfigures, the blue-dashed line shows the $t^{*1/2}$ scaling. The dot-dashed violet line in the right panel indicates the t^* scaling. Red arrows indicate the direction of time.

SI.4: BOX-TRAPPED BECS. GP SIMULATIONS

In order to study the scaling of the minimum distance δ with respect to time in further experimentally accessible geometries and with the objective of backing our interpretation of the scaling crossover outlined in the main text, we perform numerical simulations of vortex dynamics and reconnections in recently designed *box-traps* [6, 7]. The fundamental differences between box-trapped BECs and harmonically trapped BECs (investigated in the main text, see Figs. 5 and 6) are mainly two. First, in box-traps the density of the confined BEC is constant throughout the sample (exception made for a thin layer near the trap edges whose width is of the order of the healing length), while in harmonically trapped BECs the condensate density is maximum in the center of the trap and decreases parabolically when moving towards the boundaries of the trap. Second, while in box-traps the role of the vortex images with respect to trap boundaries is central in driving the motion of vortices [8], in harmonic traps the vortex dynamics is determined by density gradients (arising from the inhomogeneous trapping potential) and vortex curvature [9–11], while the role of images still remains an open question [8, 10, 12–14].

The initial vortex configuration for the two simulations performed in box-traps is illustrated in Fig. S2 (a), (b). The initial distance from the top/bottom boundary $h_0^* = h_0/\xi = 20$ is constant for both simulations (where ξ is the healing length evaluated in the bulk of the condensate, *i.e.* away from the trap boundaries), while to investigate the role of images we choose two distinct values of d_0^* : $d_0^* = 8.25$ (dark yellow squares in Fig. S3) and $d_0^* = 11.05$ (red circles in Fig. S3). The existence of image vortices drives the vortices towards each other until they reconnect. The temporal evolution of the minimum distance $\delta^* = \delta/\xi$ is reported in Fig. S3 (left). It clearly emerges that for $t^* \lesssim 10$, δ^* follows a $t^{*1/2}$ scaling indicating that when vortex cores start merging, the predominant dynamics driving the approach of the vortices is the interaction between the latter, consistently with the characteristics of vortex reconnections observed in homogeneous condensates (see Fig. 3 in main manuscript).

In addition, for $t^* \gtrsim 200$ in the approach dynamics, we again observe a linear scaling, *i.e.* $\delta^*(t^*) \sim a_1 t^*$, as in homogeneous BECs (see Fig. 3 in main manuscript), implying a constant value of $d\delta^*/dt^*$. In the present geometry, this constant projection of the relative velocity between vortices on the separation vector (*i.e.* $d\delta^*/dt^*$) coincides with the sum of the velocity magnitudes induced by the vortex images [8],

$$\begin{aligned} \frac{d\delta^*}{dt^*} &= |\mathbf{v}_2 - \mathbf{v}_1| = v_{2,img}^* + v_{1,img}^* \\ &= \frac{\kappa}{2\pi c(d_0 - \sqrt{2}\xi)} = \frac{\kappa}{2\pi c\bar{d}_0} \frac{1}{\left[\tilde{d}_0 - \frac{\sqrt{2}}{d_0^*}\right]} \\ &= Cf(\tilde{d}_0) , \end{aligned} \quad (6)$$

where: \mathbf{v}_1 (\mathbf{v}_2) is the velocity of the top (bottom) vortex; $v_{1,img}$ ($v_{2,img}$) is the velocity of the top (bottom) vortex induced by the corresponding image with respect to the lateral boundary of the trap at a distance d_0 (cfr. Fig. S2 (a), (b)); $\tilde{d}_0 = d_0/\bar{d}_0$, $\bar{d}_0 = 9.65\xi$ being the average distance to the lateral boundary of the trap amongst the two simulations performed in box-traps; ξ is the healing length based on the bulk density $n = \mu/g$, with μ and g being the chemical potential and the repulsive interaction strength, respectively; $c = \sqrt{gn/m}$ is the speed of sound; $C = \frac{\kappa}{2\pi c d_0}$ is a non-dimensional constant independent

of d_0 and $f(\tilde{d}_0) = \left[\tilde{d}_0 - \frac{\sqrt{2}}{d_0^*}\right]^{-1}$ is a non-dimensional function depending on the distance d_0 .

Hence, for $t^* \gtrsim 200$ in pre-reconnection dynamics we argue that $\delta^*(t^*) \sim Cf(\tilde{d}_0)t^*$. This conjecture is confirmed in Fig. S3 (right) where we report the temporal evolution of the rescaled minimum distance $\delta^*/f(\tilde{d}_0)$ for $d_0^* = 8.25$ and $d_0^* = 11.05$: the curves do indeed overlap at large distances. The post-reconnection dynamics is less straightforward to investigate as a result of other factors playing a significant role in determining the vortex dynamics, above all acoustic emission and vortex pinning on the boundaries of the trap (as it can be observed in movies M4).

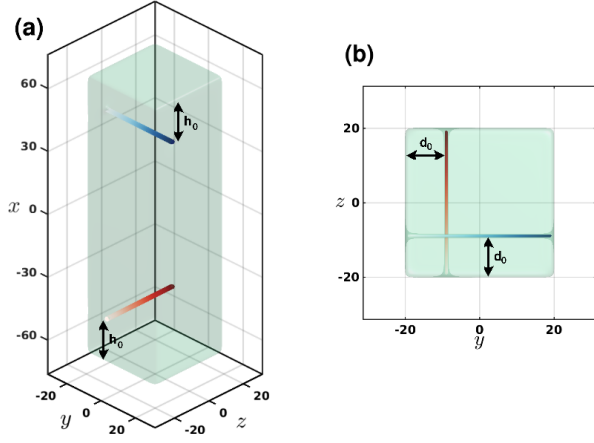


FIG. S2. GP simulations: box-trapped BECs, initial conditions. (a), (b): Lateral and top view of initial vortex configuration for box trapped BECs; Light green surfaces coincide with isosurfaces of condensate density at 5% of trap-center density. Color gradient on vortices indicates the direction of the superfluid vorticity (from light to dark). Unit of length is the healing length ξ evaluated in the bulk of the condensate.

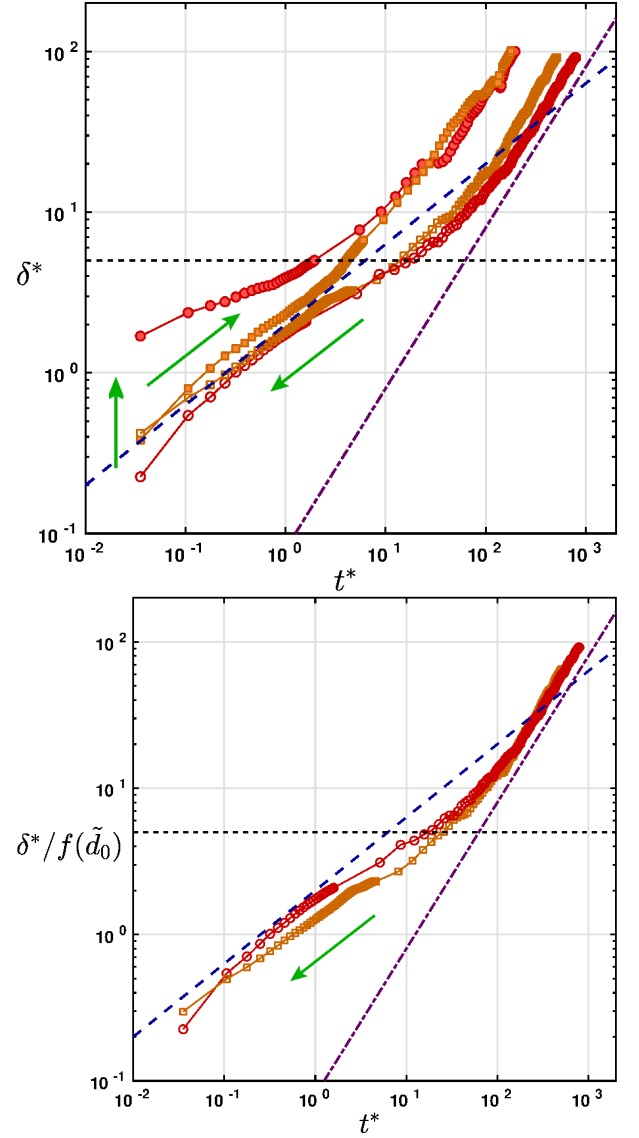


FIG. S3. GP simulations: box trapped BECs. Evolution of the minimum distance δ^* between reconnecting vortices as a function of the temporal distance to reconnection t^* . Open (filled) symbols correspond to pre (post) reconnection dynamics. **Left:** pre- and post-reconnection scaling of δ^* for initially imprinted orthogonal vortices at distance d_0^* from trap lateral boundaries and h_0^* from top/bottom boundaries (see Fig.S2): $d_0^* = 8.25$ (\square), $d_0^* = 11.05$ (\circ); $h_0^* = 20$ for both simulations. **Right:** pre-reconnection scaling of rescaled minimum distance $\delta^*/f(\tilde{d}_0)$. Symbols as in left panel. In both subfigures, the dashed blue and dot-dashed violet lines show the $t^{*1/2}$ and t^* scalings, respectively. The horizontal black dashed line indicates the width of the vortex core ($\approx 5\xi$). Green arrows indicate the direction of time.

METHODS

SI.5: Numerical methods for GP simulations

Real-time dynamical simulations of vortex dynamics in BECs at temperature $T = 0$ are performed by numerically integrating the mean-field Gross-Pitaevskii (GP) equation,

$$i\hbar \frac{\partial \Psi}{\partial t} = -\frac{\hbar^2}{2m} \nabla^2 \Psi + V\Psi + g|\Psi|^2\Psi \quad (7)$$

for the complex macroscopic wave function $\Psi(x, y, z, t)$, where m is the boson mass, V is the external potential and $g = 4\pi\hbar^2 a_s/m$ is the strength of the repulsive two-body interaction, a_s being the atomic scattering length.

Our code uses second-order accurate finite differences in space and a fourth order Runge–Kutta method in time.

The algorithm for vortex tracking is based on the pseudo-vorticity unit vector

$$\hat{\omega} := \frac{\nabla\Psi_{\Re} \times \nabla\Psi_{\Im}}{|\nabla\Psi_{\Re} \times \nabla\Psi_{\Im}|}$$

which is tangent to the vortex line along its length [15, 16], where $\Psi = \Psi_{\Re} + i\Psi_{\Im}$.

Homogeneous BECs. In homogeneous systems, the external potential V is zero and the wave function Ψ is normalized by $\Psi_0 = \sqrt{n}$, where $n = \mu/g$ is the homogeneous density of an unbounded BEC in its ground state. By writing $\Psi^* = \Psi/\Psi_0$ and introducing the healing length $\xi = \hbar/\sqrt{2mgn}$ as the unit of length and $\tau = \xi/c$ as the unit of time, where $c = \sqrt{gn/m}$ is the velocity of sound, we obtain the following non-dimensional GP equation:

$$i \frac{\partial \Psi^*}{\partial t^*} = -\frac{1}{2} \nabla^{*2} \Psi^* + \frac{1}{2} |\Psi^*|^2 \Psi^* \quad (8)$$

where the superscript ‘*’ indicates non-dimensional variables. Hereafter all the quantities mentioned are dimensionless, unless otherwise stated, and the superscript ‘*’ is omitted to ease notation.

Orthogonal vortices. We imprint two orthogonal vortices: the first is oriented in the negative z direction, the second in the negative y direction. The vortices intersect the x axis at $(-x_0, 0, 0)$ and $(x_0, 0, 0)$ respectively. We compare runs with $x_0 = 5, 10, 15$ leading to initial distances $\delta_0 = 10, 20, 30$ (see the bottom inset in Fig. 3 (left) of the main manuscript). Spatial and time discretization use steps $\Delta x = \Delta y = \Delta z = 0.35$ and $\Delta t = 0.02$. The number of grid-points in the x , y and z direction are $\{N_x, N_y, N_z\} = \{400, 400, 400\}$ respectively, leading to a computational box $\{[x_{\min} : x_{\max}] \times [y_{\min} : y_{\max}] \times [z_{\min} : z_{\max}]\}$ =

$$\{[-70 : 70] \times [-70 : 70] \times [-70 : 70]\}.$$

Ring - line reconnection. We perform simulations for a vortex ring of radius $R_0 = 5, 7.5$ and 10 , and centre $(x_0, y_0, z_0) = (-100, 21, 0)$ on a plane perpendicular to the x direction. The line is oriented in the positive z direction and intersects the y axis at $(x_1, y_1, z_1) = (0, 21, 0)$, as shown in the bottom inset of Fig. 3 (right) in the main manuscript.

The spatial and temporal resolution coincides with orthogonal vortices simulations. The numbers of grid-points in the x , y and z directions are $N_x = 800$, $N_y = 280$ and $N_z = 160$ respectively, leading to a larger computational box: $-140 \leq x \leq 140$, $-50 \leq y \leq 50$ and $-28 \leq z \leq 28$.

Trapped BECs. For harmonically trapped, cigar-shaped BECs the units of length, time and energy are $\ell_{tr} = \sqrt{\hbar/(m\omega_{\perp})}$, $\tau = \omega_{\perp}^{-1}$ and $\epsilon = \hbar\omega_{\perp}$, respectively, where ω_{\perp} is the radial trapping frequency of the harmonic potential. The resulting non-dimensional GP equations is

$$i \frac{\partial \tilde{\Psi}}{\partial t} = -\frac{1}{2} \tilde{\nabla}^2 \tilde{\Psi} + \tilde{V} \tilde{\Psi} + \tilde{g} |\tilde{\Psi}|^2 \tilde{\Psi} \quad (9)$$

where with $\tilde{\cdot}$ we indicate non-dimensional quantities, $\tilde{\Psi}$ is normalized to unity ($\int_V |\tilde{\Psi}|^2 dV = 1$ where V is the volume), and $\tilde{g} = 4\pi N a_s / \ell_{tr}$ and N is the number of atoms in the condensates. Hereafter all the quantities which we mention are meant to be dimensionless unless otherwise stated, and the superscript $\tilde{\cdot}$ is omitted to ease notation.

Box Traps. We choose $g = 2.35 \times 10^4$ and set the trapping potential to

$$V = \begin{cases} 0 & \text{for } |x| < L_x/2 \text{ and } |y| < L_y/2 \text{ and } |z| < L_z/2 \\ 10\mu & \text{elsewhere} \end{cases} \quad (10)$$

where $\mu = 10$ is the chemical potential, $L_x = 29.46\ell_{tr} = 131.75\xi$ and $L_y = L_z = 8.944\ell_{tr} = 40\xi$, ξ being the healing length in the bulk of the condensate.

In Fig. S2 (a), (b), the distance of vortices from the top/bottom edge of the trap is $h_0 = 4.48\ell_{tr} = 20\xi$, leading to the initial minimum distance between vortices $\delta_0 = 20.5\ell_{tr} = 91.75\xi$. The distance of the vortices from the lateral edges is $d_0 = 1.48\ell_{tr} = 8.25\xi$ and $d_0 = 2.47\ell_{tr} = 11.05\xi$. The top vortex is oriented in positive y direction and the bottom vortex is the positive z direction.

The grid-spacings are homogeneous in the three Cartesian directions, $\Delta x = \Delta y = \Delta z = 7.5 \times 10^{-2}$, and the time step is $\Delta t = 1.25 \times 10^{-3}$. The numbers of

grid-points in the x , y and z directions are $N_x = 512$, $N_y = 192$ and $N_z = 192$, leading to the computational box $-19.2 \leq x \leq 19.2$, $-7.2 \leq y \leq 7.2$ and $-7.2 \leq z \leq 7.2$.

Harmonic Traps. We choose $g = 7.4 \times 10^3$ and $\mu = 10$. The trapping potential is

$$V = \frac{1}{2} \left[\left(\frac{\omega_x}{\omega_\perp} \right)^2 x^2 + r_\perp^2 \right] \quad (11)$$

where $\omega_x = 2\pi \times 26$ Hz is the axial trapping frequency, $\omega_\perp = \omega_y = \omega_z = 2\pi \times 131$ Hz is the radial trapping frequency, and $r_\perp = (y^2 + z^2)^{1/2}$ is the distance from the axis of the condensate. These parameters correspond to $R_\perp/\xi_c = 2\mu/(\hbar\omega_\perp) = 20$, where R_\perp is the radial Thomas-Fermi radius and ξ_c is the healing length evaluated in the center of the trap.

We imprint two orthogonal vortices as shown in Fig. 5 of main text; the top vortex is oriented in the negative y direction, the bottom in the negative z direction. The vortices intersect the x axis at $(\pm x_0, 0, 0)$, where $x_0 = \chi R_x$, $\chi = 0.35, 0.5, 0.6$ is the orbit parameter, and R_x is the axial Thomas-Fermi radius.

Spatial and temporal resolutions coincide with the box-trap simulations. The numbers of grid-points in the x , y and z directions are $N_x = 800$, $N_y = 224$ and $N_z = 224$, leading to the computational box $-30 \leq x \leq 30$, $-8.4 \leq y \leq 8.4$, and $-8, 4 \leq z \leq 8.4$.

SI.6: Numerical methods for VF simulations

The Vortex Filament method [3, 17] is a well-established model widely employed for the numerical simulations of superfluid helium quantum turbulence. A typical superfluid helium experiment is characterised by the large separation of scales between the large scale D of the flow ($D \approx 10^{-2}$ m) and the small length scale of the average inter-vortex distance $\ell_v \approx 10^{-5}$ m; the vortex core radius, $a_0 \approx 10^{-10}$ m in ^4He and about 100 times larger in $^3\text{He-B}$, is even smaller. It is therefore appropriate to mathematically model quantum vortices as closed space curves of infinitesimal thickness $\mathbf{s}(\zeta, t)$, where ζ is arclength and t time, moving in an inviscid Euler fluid according to the Biot-Savart law [18, 19],

$$\frac{\partial \mathbf{s}}{\partial t} = \frac{\kappa}{4\pi} \oint_{\mathcal{L}} \frac{\mathbf{s}'(\eta, t) \times [\mathbf{s}(\zeta, t) - \mathbf{s}(\eta, t)]}{|\mathbf{s}(\zeta, t) - \mathbf{s}(\eta, t)|^3} d\eta \quad (12)$$

where the line integration is performed along the entire vortex configuration \mathcal{L} and $\mathbf{s}'(\zeta, t) = \frac{\partial \mathbf{s}}{\partial \zeta}$ is the unit tangent vector.

Vortex-lines are discretised in sets of points $\mathbf{s}_i(t) = \mathbf{s}(\zeta_i, t)$, $i = 1 \dots N$, with initial spatial discretisation

$\Delta\zeta = 5 \times 10^{-5}$ m. The Lagrangian dynamics of the vortex points is hence obtained evaluating the discretised Biot-Savart integral starting from a given initial vortex configuration. The singularity of the Biot-Savart integral for $\eta \rightarrow \zeta$ is fixed by taking into account the finite size of the vortex core, yielding [18, 20] the following decomposition between local and non-local contributions:

$$\begin{aligned} \frac{\partial \mathbf{s}}{\partial t} &= \frac{\kappa}{4\pi} \mathbf{s}'(\zeta) \times \mathbf{s}''(\zeta) \ln \left(\frac{2\sqrt{l_+ l_-}}{e^{1/2} a_0} \right) + \\ &+ \frac{\kappa}{4\pi} \oint_{\mathcal{L}'} \frac{\mathbf{s}'(\eta) \times [\mathbf{s}(\zeta) - \mathbf{s}(\eta)]}{|\mathbf{s}(\zeta) - \mathbf{s}(\eta)|^3} d\eta, \end{aligned} \quad (13)$$

where time dependence has been omitted to ease notation, \mathbf{s}'' is the normal vector at $\mathbf{s}(\zeta)$, l_\pm are the lengths of the line segments connected to $\mathbf{s}(\zeta)$ after discretisation, and the integral is evaluated on \mathcal{L}' , the original vortex configuration \mathcal{L} without the line segments adjacent to $\mathbf{s}(\zeta)$.

Reconnections are not intrinsically predicted by the VF method, as Euler inviscid dynamics forbids such changes of topology. As a consequence, an additional algorithm has to be employed which changes the topology of the vortex configuration when two vortex lines become closer than an arbitrary threshold distance which in this work we set to $\Delta\zeta/2$. Moreover, in order to model the dissipative nature (phonon emission) of reconnecting events [21], the numerical *cut and paste* reconnection algorithm reduces vortex length (which is taken as a proxy for the kinetic energy of the vortices). It is important to stress, in fact, that given the length-scales of the flow investigated (much larger than the characteristic length-scale of density variations in superfluid helium), the VF method is an incompressible model. Several reconnections algorithms have been introduced in VF method literature. Importantly, a recent analysis [5] has showed that all these algorithms produce very similar results, at least in the context of superfluid turbulence.

The number of discretization points, N , changes with time as the simulation progresses (discretization points are introduced or removed to maintain the numerical resolution along the vortex filaments.) In the present study, if the separation between two discretization points becomes greater than $\Delta\zeta$, a new intermediate point is inserted with the constraint of preserving the vortex curvature. Similarly, if the separation becomes less than $\Delta\zeta/2$, points are removed in order to ensure that our shortest scale which is numerically resolved does not change [22].

In the present work, time integration is performed employing a third order Runge-Kutta method with time step $\Delta t = 5 \times 10^{-4}$ s, while all spatial derivatives are approximated using fourth-order finite difference schemes which account for varying mesh sizes along the vortex filaments [22, 23].

Movies

M1

Videos M1.A, M1.B, M1.C and M1.D are a rendering of the reconnection of orthogonal vortices with initial minimum distance $\delta_0^* = 10$, computed employing the Gross-Pitaevskii (GP) model.

M2

Videos M2.A, M2.B, M2.C and M2.D are a rendering of the reconnection between a vortex ring and a vortex line with initial minimum distance $\delta_0^* = 100$ and initial vortex ring radius $R_0^* = 5$, computed employing the GP model.

M3

Videos M3.A and M3.B are a rendering of the reconnection between vortex lines in a harmonically trapped Bose-Einstein condensate corresponding to an orbit parameter $\chi = 0.35$, computed employing the GP model.

M4

Videos M4.A and M4.B are a rendering of the reconnection between vortex lines in a box-trapped Bose-Einstein condensate corresponding to an initial lateral distance from the trap boundary $d_0^* = 11.05$, computed employing the GP model.

M5

Videos M5.A and M5.B are a rendering of the reconnection of orthogonal vortices with initial minimum distance $\delta_0^* = 2.5 \times 10^6$, computed employing the Vortex Filament (VF) method.

M6

Videos M6.A and M6.B are a rendering of the reconnection between a vortex ring and a vortex line with initial minimum distance $\delta_0^* = 2 \times 10^7$ and initial vortex ring radius $R_0^* = 1.2 \times 10^7$, computed employing the VF method.

- [1] E. Buckingham, *Phys Rev* **4**, 345 (1914).
- [2] P. H. Roberts and J. Grant, *J Phys A: Gen Phys* **4**, 55 (1971).
- [3] R. Hänninen and A. W. Baggaley, *Proc Natl Acad Sci USA*, 201312535 (2014).
- [4] A. De Waele and R. Aarts, *Phys Rev Lett* **72**, 482 (1994).
- [5] A. W. Baggaley, *J Low Temp Phys* **168**, 18 (2012).
- [6] A. Gaunt, T. Schmidutz, I. Gotlibovych, and Z. Smith, R P.Hadzibabic, *Phys Rev Lett* **110**, 200406 (2013).
- [7] N. Navon, A. Gaunt, and Z. Smith, R P.Hadzibabic, *Nature* **539**, 72 (2016).
- [8] P. Mason, N. Berloff, and A. Fetter, *Phys Rev A* **74**, 043611 (2006).
- [9] A. Svidzinsky and A. Fetter, *Phys Rev Lett* **84**, 5919 (2000).
- [10] A. Fetter and A. Svidzinsky, *J. Phys.: Condens. Matter* **13**, R135 (2001).
- [11] B. Jackson, J. McCann, and C. Adams, *Phys Rev A* **61**, 013604 (1999).
- [12] J. Anglin, *Phys Rev A* **65**, 063611 (2002).
- [13] U. A. Khawaja, *Phys Rev A* **71**, 063611 (2005).
- [14] A. Fetter, *Rev Mod Phys* **81**, 647 (2009).
- [15] C. Rorai, J. Skipper, R. Kerr, and K. Sreenivasan, *J Fluid Mech* **808**, 641 (2016).
- [16] A. Vilhois, D. Proment, and G. Krstulovic, *Phys Rev Fluids* **2**, 044701 (2017).
- [17] K. Schwarz, *Phys Rev B* **38**, 2398 (1988).
- [18] K. Schwarz, *Phys Rev B* **31**, 5782 (1985).
- [19] P. G. Saffman, *Vortex dynamics* (Cambridge University Press, 1992).
- [20] R. Arms and F. R. Hama, *Phys Fluids* **8**, 553 (1965).
- [21] M. Leadbeater, T. Winiecki, D. Samuels, C. Barenghi, and C. Adams, *Phys Rev Lett* **86**, 1410 (2001).
- [22] A. W. Baggaley and C. F. Barenghi, *Phys Rev B* **83**, 134509 (2011).
- [23] L. Gamet, F. Ducros, F. Nicoud, and T. Poinso, *Int J Num Meth Fluids* **29**, 159 (1999).

* luca.galantucci@newcastle.ac.uk